Optimisation of a dynamic absorber with nonlinear stiffness and damping for the vibration control of a toy model for floating offshore wind turbine

Pierre-Olivier Mattei, Renaud Côte

Optimisation of a dynamic absorber with nonlinear stiffness and damping for the vibration control of a toy model for floating offshore wind turbine

Pierre-Olivier Mattei[1] and Renaud Côte[1]

[1] Aix Marseille Univ, CNRS, Centrale Marseille, LMA UMR 7031, 4 impasse Nikola Tesla, CS 40006,13453 Marseille Cedex 13, France

Passive vibration mitigation of offshore wind turbines using nonlinear absorbers or nonlinear energy sinks has started to receive attention in the literature. In most cases, little attention has been paid to the possibility of detached resonances that occur when the nonlinear energy sink is attached to the linear system describing the wind turbine. Sea motions that alter the initial conditions of the floating offshore wind turbine may cause the nonlinear energy sink to operate at one or more detached resonances, completely negating its ability to control turbine vibration. In this paper, we are interested in optimizing the parameters of a nonlinear energy sink with nonlinear stiffness and nonlinear viscous damping for vibration control of a toy model (e.g., a linear mass-spring-damper system) of a floating offshore wind turbine over its entire operating range. The mechanism of cancellation of the detached resonance is studied analytically under 1:1 resonance. It is shown that the nonlinear energy sink with properly tuned nonlinear viscous damping allows the complete elimination of undesired regimes and completely restores the absorber's ability to strongly limit the vibration of a floating offshore wind turbine over its entire forcing range. The results obtained over a wide range of parameters suggest that both the optimal nonlinear energy sink parameters (linear and nonlinear stiffness and nonlinear damping) and the damping of floating offshore wind turbine vibration depend on simple power laws of nonlinear energy sink mass and linear damping.

Keywords Passive vibration reduction, nonlinear energy sink, geometrically nonlinear damping, floating offshore wind turbine.

1 Introduction

Renewable wind energy is developing rapidly these days. Offshore wind turbines are particularly adapted to generate high power in different environmental conditions. In fact, they are subject to more regular wind conditions than in the land and the possibility of developing large wind turbines that are more efficient from the energy point of view, using slender towers and extremely long blades, and less disturbing to local residents and fauna. Among these, Floating Offshore Wind Turbines (FOWTs) are easy to implement in deep water farms and are likely to develop strongly in the coming years. This type of wind turbine is gigantic in size (with a height of almost 100 m and 150 m with the blades), very heavy (with a mass of almost 1000 tons) and has dynamic characteristics that are difficult to control. Most wind turbine primary resonances are below 1 Hz (typically 0.3 Hz to 0.5 Hz) and have very low intrinsic damping. FOWTs are subjected to various types of dynamic loads, such as environmental loads (wave and wind), aero-structure interaction loads, and mechanical loads (inertial and controller effects). These loads induce vibrations in the wind turbine tower, which are transmitted to the floating foundation and mooring lines, increasing the overall ultimate loads and fatigue cycles.

Mitigating the vibration of wind turbines (WTs) under dynamic loads such as wind, sea waves, earthquakes has been addressed by many researchers (see Zuo, Bi, et al. 2020). Since no external energy is required, most studies have been conducted on passive linear devices, such as single (TMDs) or multiple tuned mass dampers (MTMDs) or tuned liquid dampers (TLDs), thanks to their ability to improve the damping of the whole system. Classically, a TMD is optimized near a specific frequency of the WT to be controlled and is effective in a narrow frequency band. Slight frequency detuning between the TMD and the controlled structure can significantly

change the efficiency of the TMD. FOWTs are often located in harsh marine environments and their natural resonances are altered not only by design and construction discrepancies, but also by operating conditions, degradation of material properties, or structural damage.

Since the first seminal work by Gendelman, Manevitch, et al. (2001) twenty years ago, the nonlinear passive dynamical absorber (also known as the nonlinear energy sink - NES), which can be viewed as an extension of Den Hartog's TMD to correct its lack of robustness to a variation of the primary system, has received increasing attention from the academia and industry. (Ding et al. 2020). NES usually consists of a small mass, a viscous damper and a pure nonlinear stiffness element. The essentially nonlinear stiffness enables system dynamics without a fixed frequency, resulting in a large frequency band capability in dissipating energy from the host structure. Therefore, NESs are robust to any structural frequency changes. As shown by Gendelman, Manevitch, et al. (2001), a restoring force of a third-order power of deformation results in a vibrational energy of the controlled structure to be irreversibly transferred to a cubic NES. Since then, many kinds of NESs have been designed, such as serial cubic NESs (Gendelman, Sapsis, et al. 2011), bi-stable NESs (AL-Shudeifat 2014), magnet-based NESs (Chen et al. 2020), vibro-impact NESs (Gourc et al. 2015), or track NESs which provide a non-linear restoring force similar to that of a cubic-like NES (Wang et al. 2015) to improve their efficiency. A particular Track-NES, which provides a nonlinear restoring force similar to that of a bistable-like NES, has recently been used by Zuo and Zhu (2022) to control earthquake-induced vibration in OWTs.

One of the main difficulties encountered when using a NES to damp oscillatory motion is that, under periodic forcing, there exists a high-amplitude detached resonance solution in the frequency response curves of oscillatory systems with non linearity that must be absolutely avoided. The occurrence of such detached resonances in nonlinear oscillators has been known for a long time (Rauscher 1938; Abramson 1955). The nonlinearity could be that of the elastic restoring force, as shown for example by Alexander et al. (2009), or that of the damping force, as shown by Habib, Cyrillo, et al. (2018). To overcome this difficulty, the parameters of the NES must be constrained in a certain range of space parameters as shown in Gourc et al. (2014). While efficient, this procedure limits the ability to maximize the attenuation obtained by the NES.

The most interesting way to overcome such detached resonance is the use of tuned nonlinear damping. As shown by Starosvetsky et al. (2009) who use a quadratic damping whose characteristics are composed of two parts: a low and a high amplitude quadratic damping which differ only by their coefficients: the damping force $f = \lambda_1 \dot{x}|\dot{x}|, x < x_{cr}$ and $f = \lambda_2 \dot{x}|\dot{x}|, x > x_{cr}$. Using Manevitch's complexification averaging under the 1: 1 resonance, the authors compute the slow invariant manifold (SIM) of the system, which allows to analyze the strongly modulated response (SMR), which is the best way to dissipate energy in such a system; they observe that the destruction of the detached resonance is achieved when the high amplitude quadratic damping coefficient λ_2 is sufficiently greater than λ_1, they gave a ratio of 12 in their example. The problem pointed out by the authors is that the optimization procedure fails when the upper detached resonance merges with the lower branch main resonance curve. It is worth noting that the main resonance curve can be viewed as the frequency response curve (FRF) of the usual linear system. Similarly, viscous nonlinear damping has been studied by Andersen et al. (2012), who define a NES consisting of a mass attached to two additional elements composed of inclined parallel linear spring-damper pairs. The transverse motion of the mass induces not only linear and cubic stiffness (which is the usual way to construct nonlinear springs and NES), but also linear and cubic viscous damping. In their work, the authors had found that due to the presence of nonlinear damping, the structure can exhibit dynamic instabilities.

This type of nonlinear damping is analogous to that observed by Bellet et al. (2010) when applying the concept of directed energy transfer to the field of acoustics, using a high-amplitude vibrating membrane as an NES. It was also used by Liu et al. (2019), who generalized the NES by allowing the inclined parallel linear spring-damper pairs to form an initial angle ϕ_0 at rest. This not only allows for high amplitude transverse motion, but also, depending on the initial angle of inclination, the dynamics of the system can be either hardened or softened at different phases of the motion. In this work, the authors observed that by using appropriate values for the NES parameter, unwanted detached resonances can be completely eliminated.

The NES model proposed by Andersen et al. (2012) is the basis of the work presented below.

In this paper, only air-structure interaction loads are considered. FOWTs operate over a wide range of wind speeds (typically between 5 and 40 knots) and their operating principle is that the blade rotation speed is essentially constant. In practice, as shown by Pahn et al. (2012) in real cases, the tower of a wind turbine is subjected to a thrust force composed of an almost constant term and a periodic force: $F(t) = A_0 + A\cos(\omega t)$, with $\omega = 2\pi f$, where f is the force frequency, which depends mainly on the wind speed variations, the speed of the FOWT and the number of blades. In the different cases considered by the authors, most of the dynamic components are below 1 Hz with a maximum amplitude of about 10 kN.

To simplify the calculations, the wind turbine is described as a linear mass-spring-damper system coupled to a NES with linear and cubic characteristics for stiffness and damping.

In this paper, we are interested in optimizing the parameters (linear and nonlinear stiffness and nonlinear damping) of the NES for the vibration control of this toy model over its entire operating range under periodic forcing.

For this purpose, a two step procedure is proposed. During the first pass, the occurrence of detached resonance is limited by imposing a zero initial condition, and for a set of fixed NES mass and linear damping, the linear and nonlinear stiffness of the NES are optimized to reduce the vibration of the FOWT over its entire forcing range. Once optimal parameters are determined, non-zero initial conditions are imposed to exhibit detached resonances and nonlinear damping is adjusted to cancel them out.

Results obtained over a large range of parameters suggest that both the optimal NES parameters (linear and nonlinear stiffness and nonlinear damping) and the attenuation of FOWT vibration depend regularly on NES mass and linear damping.

This paper is structured as follows. The second section is dedicated to the description of the problem. The third section is devoted to the presentation of the numerical method that solves the exact equations and to the introduction of the optimization under two aspects, the first by using literature results that avoid detached resonance problem and the second by showing how the optimal vibration reduction obtained by using brute force without taking into account detached resonance is completely wiped out when they appear. The fourth section is devoted to an analytical study of nonlinear damping to show that when it is used to control detached resonances, it does not alter the underlying mechanism of energy transfer. The cancellation of the detached resonance is studied analytically under 1:1 resonance. It is shown that the NES with properly tuned nonlinear viscous damping allows the complete elimination of undesired regimes and completely restores the absorber's ability to strongly limit FOWT vibration over its entire forcing range. To ensure that this nonlinear damping does not modify the dynamics of the system too much, the slow flow of the system is studied by computing its slow invariant manifold. It is shown that, while not perfectly describing all features of the exact solution, most of the characteristics of the slow flow are preserved when the nonlinear damping is taken into account. The fifth section is devoted to a synthetic presentation of the optimization results obtained by using brute force and detached resonance cancellation; it is shown that the linear, nonlinear stiffness and the nonlinear damping of the NE and attenuation of the FOWT vibrational motion depend on simple power laws of the NES mass and linear damping. The sixth section is devoted to the conclusion.

2 Equations of the problem

The wind turbine considered in this article has a resonant frequency of 0.50 Hz and a damping ζ_0 of 0.05%. The forcing frequency f considered in this paper varies over a third of an octave around 0.50 Hz (near the resonance of the wind turbine) and the force applied to the wind turbine tower A varies between $A_{min} = 3$ N and $A_{max} = 10$ kN; the minimum value of 3 N was chosen as a compromise between a maximum amplitude to ensure linear motion for the NES and a minimum amplitude to ensure numerically regular computation for the principal system (too small a forcing amplitude leads to numerical instabilities). In the following, the constant term A_0 is neglected.

Figure 1 shows the simplified idealized nonlinear system describing the FOWT together with the NES. A primary mass m_0 is attached to the ground through a linear spring k_0 and a viscous damper c_0. It is excited by an harmonic force $A\cos(\omega t)$. The NES, connected to the

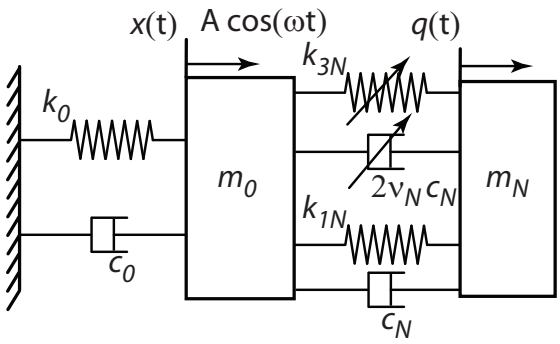

Figure 1: Model of simplified two degree-of-freedom with non-linear stiffness and nonlinear damping

primary mass, consists of oscillator of mass m_N, linear spring k_{1N}, linear viscous damperc_{1N} and nonlinear spring k_{3N} and nonlinear viscous damper $2\nu_N c_N$, all NES parameters are independent.

Let $x(t)$ be the displacement of the linear system and $q(t)$ that of the NES with $w(t) = x(t) - q(t)$. With the classical convention $\dot{x}(t) = \mathrm{d}x(t)/\mathrm{d}t$, the system with 2 degrees of freedom (2 d-o-f) is written as

$$m_0\ddot{x}(t) + c_0\dot{x}(t) + k_0x(t) + c_N(1 + 2\nu_N w^2(t))\dot{w}(t) + k_{1N}w(t) + k_{3N}w(t)^3 = A\cos(\omega t) \quad (1)$$

$$m_N\ddot{q}(t) - c_N(1 + 2\nu_N w^2(t))\dot{w}(t) - k_{1N}w(t) - k_{3N}w(t)^3 = 0, \quad (2)$$

where $m_0 = 10^6$ kg is the weight of the FOWT and $k_0 \approx 10^7$ N/m is its stiffness, leading to a pulsation of $\omega_0 = \sqrt{10} \approx \pi$. A damping coefficient of $\zeta_0 = 0.05\%$ leads to a viscosity of $c_0 = 2\zeta_0 m_0\omega_0 \approx 3200$ N.s/m. m_N is the mass of the NES, k_{1N} is the linear stiffness of the NES, and k_{3N} is its cubic stiffness coefficient. c_N is the linear viscosity coefficient of the NES. The nonlinear viscous damping $(1 + 2\nu_N w^2(t))\dot{w}(t)$ used is derived from the work of Andersen et al. (2012); $c_N\nu_N$ is the nonlinear viscous damping coefficient.

Initial conditions must be imposed on these differential equations: $x(0) = x_0$, $\dot{x}(0) = \dot{x}_0$, $q(0) = q_0$, $\dot{q}(0) = \dot{q}_0$.

Let us define non-dimensional parameters $\Omega = \omega/\omega_0$, $\tau = \omega_0 t$, $\epsilon = m_N/m_0$, $\lambda_0 = c_0/(m_N\omega_0)$, $\lambda_N = c_N/(m_N\omega_0) = \mu_N\lambda_0$, $\delta_N = k_{1N}/(m_N\omega_0^2)$, $K_N = k_{3N}/(m_N\omega_0^2)$ and $F = A/(m_N\omega_0^2)$. The previous system is then rewritten as

$$\ddot{x}(\tau) + \epsilon\lambda_0\dot{x}(\tau) + x(\tau) + \epsilon\mu_N\lambda_0(1 + 2\nu_N w^2(\tau))\dot{w}(\tau) + \epsilon\delta_N w(\tau) + \epsilon K_N w(\tau)^3 = \epsilon F\cos(\Omega\tau) \quad (3)$$

$$\epsilon\ddot{q}(\tau) - \epsilon\mu_N\lambda_0(1 + 2\nu_N w^2(\tau))\dot{w}(\tau) - \epsilon\delta_N w(\tau) - \epsilon K_N w(\tau\tau)^3 = 0 \quad (4)$$

The solution of this system can be calculated numerically without difficulty. For example, under a laptop workstation, the numerical solution using the NSolve Wolfram Research, Inc. (2021) function takes a fraction of a second for each amplitude-frequency pair for a calculation carried out over a forcing duration of more than an hour.

3 Optimisation of the exact equations

3.1 Optimisation using rules of the literature

A first optimization, taking into account only the linear component of the damping, was performed using rules from the literature, such as the one proposed for K_N by Starosvetsky et al. (2008). The chosen parameters, which avoid the problem of detached resonance by the procedure described in Gourc et al. (2014), were set as follows: $\epsilon = 0.01$, $\lambda_0 = 0.1$, $\mu_N = 2$, $\delta_N = 0.03$ and $K_N = 28$. The amplitude-frequency response surface covering 1/6 of an octave on either side of the wind turbine's resonance is shown in Figure 2. In this figure, $L(A, f) = x_{rms}(A, f)/A$, where $x_{rms}(A, f)$ is the root mean square of the steady state FOWT amplitude for a given amplitude A and forcing frequency f, and $x_{rms}(A, f)$ is estimated by averaging the value of $x(\tau)$ over the last 1/2h of motion. All calculations performed in this study to solve the initial system of Equations (3) and (4) consider 101 points in frequency and 16 points in amplitude, and each of

them requires about one minute of total time using parallel computation on 16 cores of a Dell Poweredge R640 workstation.

In Figure 2 and all figures here, all level results are given in decibels, calculated as $20\log(|L|/L_r)$, where $L_r = 1$ is the reference level. The left sub-figure in Figure 2 corresponds to the surface response over the whole amplitude and frequency range, and the right sub-figure corresponds to the ridge curve with free and blocked NES (to see its efficiency). The ridge curve is obtained by taking, for each amplitude, the maximum frequency response over the considered frequency range; this is mandatory because for such a nonlinear system the frequency of the maximum frequency response varies with the forcing amplitude; obviously, when the NES is blocked, the maximum amplitude is constant. The ridge curve shows a quasi-linear decrease in amplitude, which is the usual effect of the NES acting as an amplitude limiter over its efficiency range.

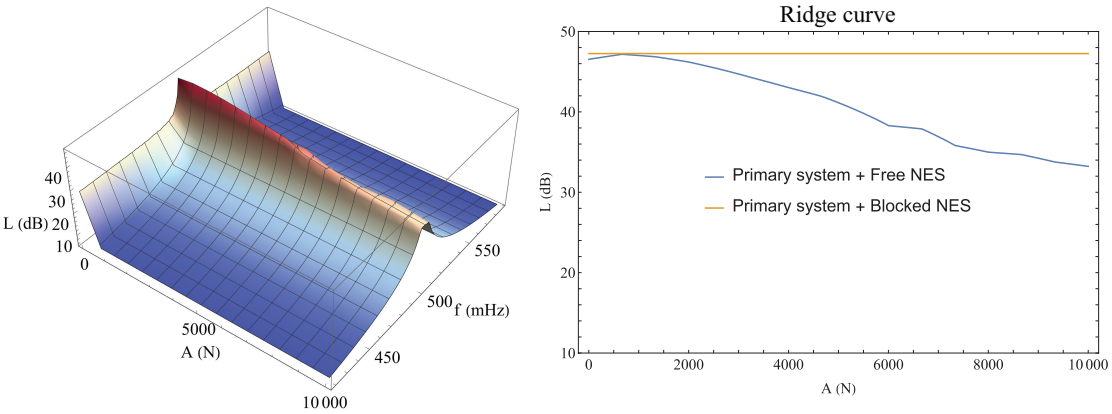

Figure 2: Frequency response of the wind turbine with $f_0^r = 0.5$ Hz with NES. Left: 3D surface response. Right: ridge curve.

These results are compared with those of an optimized tuned mass damper (TMD) with the same mass as the NES to control the resonance at 0.5 Hz. Many expressions for the parameters (δ_{TMD} characterizes the linear stiffness and μ_{TMD} the linear damping) are available in the literature since the pioneering work of Den Hartog (1947). The TMD parameters used, valid for an undamped system, as is almost the case for the FOWT under consideration, are those proposed by Bakre et al. (2007):

$$\delta_{TMD} = \frac{2+\epsilon}{2(1+\epsilon)^2}, \mu_{TMD} = \frac{1}{\lambda_0}\sqrt{\frac{\epsilon(3\epsilon+4)}{8(1+\epsilon)(2+\epsilon)}}. \tag{5}$$

The comparison is shown in Figure 3. In this figure and in following, the damping, is represented as the inverse of the gain $G(A)$ provided by the NES and by a TMD: a negative value of the gain indicates a decrease in the vibration level and then a damping, while a positive value indicates an increase in the vibration level. The different gain curves are simply the ridge curves of the FOWT normalized by its amplitude, in decibels, at its main resonance, without taking into account the nonlinear components for the NES (*i.e.* a 2 d-o-f linearly damped linear system). The TMD characteristics given by the Equations (5) are, for the considered FOWT, $\epsilon = 0.01$, $\delta_{TMD} = 0.985$ and $\mu_{TMD} = 0.498$. For each amplitude A, the level $G(A)$ of the normalized ridge curve is defined by $G(A) = \max_f L(A,f)/\left(A \max_f L_{\text{lin}}(f)\right)$, where $\max_f L_{\text{lin}}(f)$ is the maximum amplitude of the corresponding linear system obtained by canceling the nonlinear part of the NES characteristics in Equations (1) and (2). The attenuation allowed by the TMD is calculated in a similar manner and remains constant over the entire amplitude range.

In the example shown in Figure 3, the maximum amplitude of the 2 d-o-f system is reached at the resonant frequency of the FOWT without NES, near 0.5 Hz. However, since $\delta_N = 0.03$, the linear resonant frequency of the NES is $0.5 \times \sqrt{\delta_N} \approx 0.09$ Hz is outside the plotted range.

These results are satisfactory, with a maximum reduction in vibration level $-20\log|G|$ of 14 dB and an average of 5.3 dB. The goal of the optimization in the next sections is to achieve higher

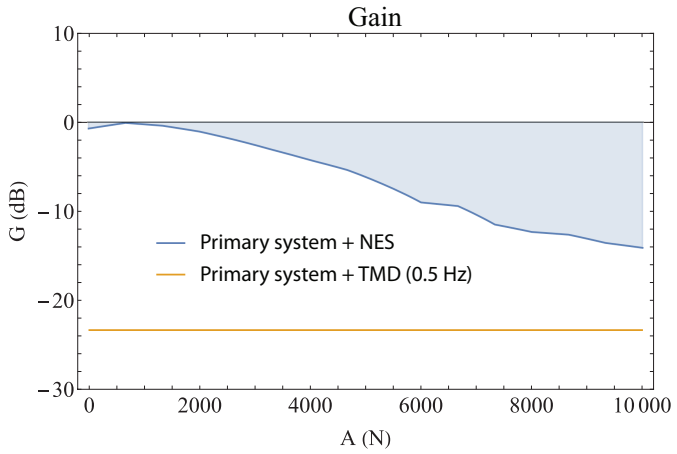

Figure 3: Attenuation (*i.e.* inverse of gain) for NES and TMD optimized for 0.5 Hz resonance

attenuation. For the current configuration, the TMD provides a much better reduction of 23.3 dB, so the goal is to get as close to the TMD result as possible.

3.2 Brute Force Optimization: Problem of Detached Resonances

Among the possible functional choices, it was chosen to minimize the mean of the $G(A)$ ridge curve to obtain the highest mean attenuation. It corresponds to the shaded area shown in Figure 3. At this stage, in order to try to avoid detached resonances, the initial conditions are set to zero for each calculation: $x_0 = 0$, $\dot{x}_0 = 0$, $q_0 = 0$ and $\dot{q}_0 = 0$.

Minimizing only for the highest forcing excitation, $A_{max} = 10000$ N in the present study, would have been too irrelevant since, in many cases, detached resonances appear around A_{max} even for zero initial conditions and transform the minimization process into a non-convergent one.

Then the functional J to be minimized is defined as

$$J = \frac{1}{A_{max} - A_{min}} \int_{A_{min}}^{A_{max}} G(A) \mathrm{d}A \tag{6}$$

Without constraints on the parameters (ϵ, μ_N, δ_N, K_N), all optimizations systematically increased the mass of the NES ϵ and decreased its damping μ_N. The solution is to fix the pair of parameters ϵ and μ_N and to optimize for each pair δ_n and K_N. The optimization, for two parameters, in Mathematica (Wolfram Research, Inc. 2021) uses a Nelder-Mead type algorithm and requires between 2 and 3 days of parallel computation using 16 cores on a Dell Poweredge R640 workstation.

For example, $\epsilon = 0.02$ and $\mu_N = 0.2$, leads to the optimal parameters $\delta_n = 0.5$ and $K_N = 43$ with an average attenuation $-20 \log |J|$ of 16.1 dB and a maximum attenuation achieved at $A = A_{max}$, $-G(A_{max}) = 28.1$ dB, compared to the 31 dB attenuation provided by the TMD observed in the Figure 4, the TMD characteristics given by the Equations (5) for this case are $\delta_{TMD} = 0.97$ and $\mu_{TMD} = 1.4$. It is worth noting that a classic result from the literature (Habib and Romeo 2020) is recovered, for which the TMD and the NES, although relying on different mechanical properties, have similar performance when the NES is optimized for a given forcing.

Of course, if the possibility of one or more detached resonances is taken into account by imposing non-zero initial conditions: $x_0 = 0.1$, $\dot{x}_0 = 0.1$, $q_0 = 0$ and $\dot{q}_0 = 0$, the results change dramatically as shown in Figure 5. Many high amplitude detached resonances appear and the NES has no more vibration reduction.

4 Nonlinear damping as a controller of detached resonance: analytical study

Before optimize the non-linear damping parameter ν_N, it must be checked that this type of damping does not modify the nature of the solution. To do so, under the assumption that the

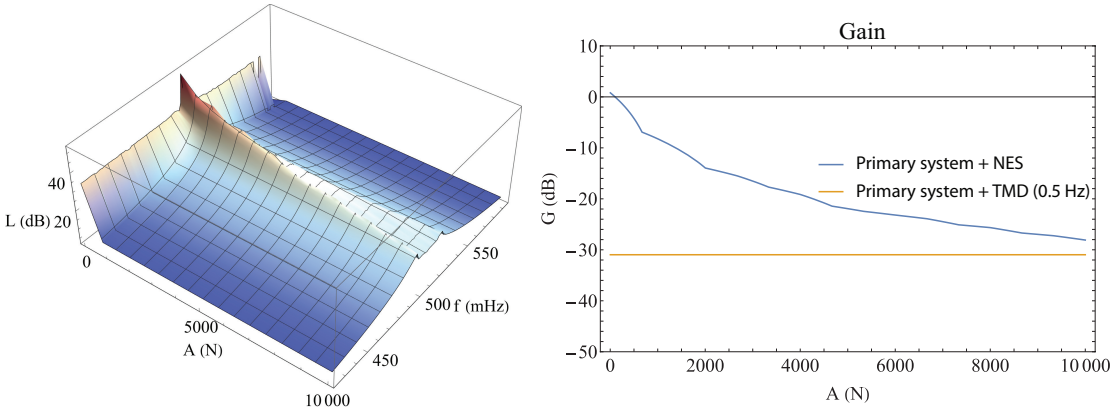

Figure 4: Optimal attenuation for $\epsilon = 0.02$ and $\mu_N = 0.2$

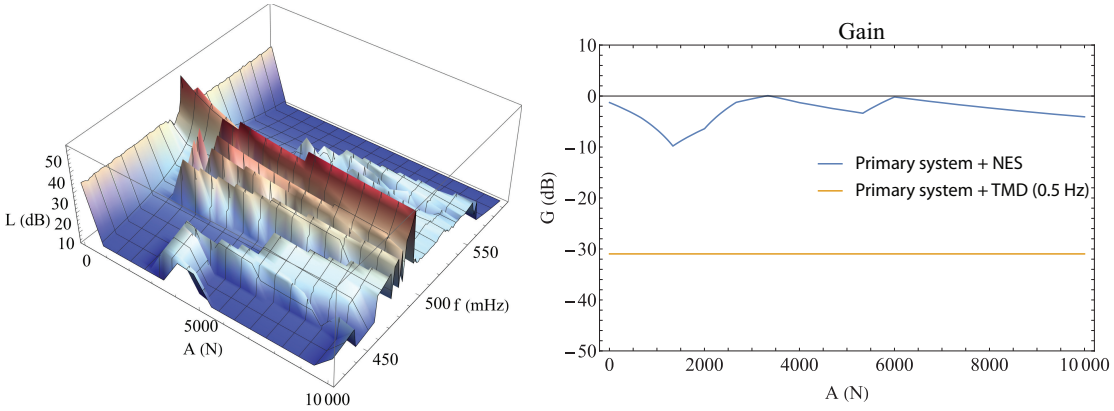

Figure 5: Attenuation for $\epsilon = 0.02$, $\mu_N = 0.2$, $\delta_n = 0.5$ and $K_N = 43$ with detached resonance

motion is under $1:1$ resonance, the fixed points and the Slow Invariant Manifold (SIM) of the system are calculated.

4.1 Fixed points

Under $1:1$ resonance, the Manevitch complexification-averaging (CX-A) method, see e.g. chapter 6 in (Vakakis et al. 2008), is applied. We start from the initial system formed by the Equations (3) and (4) in which the change of variable $v = x + \epsilon q$ is introduced. This leads to

$$\ddot{v} + \frac{v + \epsilon w}{1+\epsilon} + \epsilon\lambda_0 \frac{\dot{v} + \epsilon\dot{w}}{1+\epsilon} = \epsilon F \cos(\Omega\tau) \tag{7}$$

$$\ddot{w} + \frac{v + \epsilon w}{1+\epsilon} + \epsilon\lambda_0 \frac{\dot{v} + \epsilon\dot{w}}{1+\epsilon} + \delta_N(1+\epsilon)w + \mu_N\lambda_0(1+\epsilon)(1+2\nu_N w^2)\dot{w} + K_N(1+\epsilon)w^3 = \epsilon F \cos(\Omega\tau) \tag{8}$$

By CX-A, the new variables $\Phi_1 \exp(\imath\Omega\tau) = \dot{v} + \imath\Omega v$ and $\Phi_2 \exp(\imath\Omega\tau) = \dot{w} + \imath\Omega w$ are introduced in the preceding system and by averaging over the frequency Ω the following system of equations is obtained

$$\dot{\Phi}_1 + \imath\frac{\Omega}{2}\Phi_1 + \frac{1}{2(1+\epsilon)}\left(\epsilon\lambda_0 - \frac{\imath}{\Omega}\right)(\Phi_1 + \epsilon\Phi_2) = \epsilon\frac{F}{2} \tag{9}$$

$$\dot{\Phi}_2 + \imath\frac{\Omega}{2}\Phi_2 + \frac{1}{2(1+\epsilon)}\left(\epsilon\lambda_0 - \frac{\imath}{\Omega}\right)(\Phi_1 + \epsilon\Phi_2) - \imath\delta_N\frac{(1+\epsilon)}{2\Omega}\Phi_2 + \mu_N\lambda_0\frac{(1+\epsilon)}{2}\Phi_2 - \frac{3\imath K'_N}{8\Omega^3}(1+\epsilon)|\Phi_2|^2\Phi_2 = \epsilon\frac{F}{2} \tag{10}$$

with $K'_N = K_N\left(1 - \nu_N\mu_N\lambda_0\frac{2\Omega}{3\imath K_N}\right)$. It is easy to see that taking into account the non-linear damping leads to a simple modification of the non-linear stiffness term under the usual form of an imaginary frequency dependent term. It is worth noting that this system represents the slow flow of the steady-state dynamics under condition of 1:1 resonance.

The fixed points $\Phi^0_{1,2}$ are solutions of the slow flow for $\dot{\Phi}_{1,2} = 0$. They are given by:

$$\Phi^0_1 = \frac{\imath\epsilon\Phi^0_2 + \epsilon F(1+\epsilon)\Omega - \epsilon^2\lambda_0\Phi^0_2\Omega}{\imath(\Omega^2-1) + \epsilon\Omega(\imath\Omega+\lambda_0)}, \tag{11}$$

$$\Phi^0_2 \text{ solution of equation } 1 + c_1\,\Phi^0_2 + c_2\,\Phi^0_2|\Phi^0_2|^2 = 0, \tag{12}$$

where the coefficient A and B are given by

$$\begin{aligned} c_1 &= \frac{1}{F\epsilon\Omega^3}\left(-\imath\delta_N + \lambda_0\Omega\left(\mu_N + \epsilon\delta_N\right) + \imath\Omega^2\left(1 + (1+\epsilon)\delta_N - \epsilon\lambda_0^2\mu_N\right)\right. \\ &\qquad \left. -\lambda_0\Omega^3\left(\epsilon + (1+\epsilon)\mu_N\right) - \imath\Omega^4\right), \end{aligned} \tag{13}$$

$$c_2 = \frac{3K'_N\left(-\imath + \epsilon\lambda_0\Omega + \imath(1+\epsilon)\Omega^2\right)}{4\epsilon F\Omega^5}. \tag{14}$$

To be solved, Equation (12) is transformed into a polynomial in $|\Phi^0_2|$ as

$$1 + a_1|\Phi^0_2|^2 + a_2|\Phi^0_2|^4 + a_3|\Phi^0_2|^6 = 0, \tag{15}$$

where the real coefficients of this polynomial are given by

$$a_1 = -|c_1|^2, \tag{16}$$

$$a_2 = -|c_1 + c_2|^2 + |c_1|^2 + |c_2|^2, \tag{17}$$

$$a_3 = -|c_2|^2. \tag{18}$$

The polynomial of degree 3 in $|\Phi^0_2|^2$ given in Equation (12) possesses one or three real roots that depend on the system parameters. Stability of these roots is obtained by an usual linearisation of a complex perturbation around the fixed points. Roughly, it consists in adding small perturbation around fixed points

$$\Phi_1 = \Phi^0_1 + \rho_1, \tag{19}$$

$$\Phi_2 = \Phi^0_2 + \rho_2. \tag{20}$$

The change of variables given in Equations (19) and (20) is introduced in the averaged system composed by Equations (9) and (10). After linearisation, one is left with the following system

$$\begin{pmatrix} \dot{\rho}_1 \\ \dot{\rho}_2 \\ \dot{\rho}^\star_1 \\ \dot{\rho}^\star_2 \end{pmatrix} = \begin{pmatrix} A_{11} & A_{12} & 0 & 0 \\ A_{21} & A_{22} & 0 & A_{24} \\ 0 & 0 & A^\star_{11} & A^\star_{12} \\ 0 & A^\star_{24} & A^\star_{21} & A^\star_{22} \end{pmatrix} \begin{pmatrix} \rho_1 \\ \rho_2 \\ \rho^\star_1 \\ \rho^\star_2 \end{pmatrix} \tag{21}$$

where the $z^\star$ denotes the complex conjugate of z. The coefficients of the matrix are given by:

$$A_{11} = -\imath\frac{\Omega}{2} - \frac{1}{2(1+\epsilon)}\left(\epsilon\lambda_0 - \frac{\imath}{\Omega}\right) \tag{22}$$

$$A_{12} = \epsilon A_{21} \tag{23}$$

$$A_{21} = -\frac{1}{2(1+\epsilon)}\left(\epsilon\lambda_0 - \frac{\imath}{\Omega}\right) \tag{24}$$

$$A_{22} = -\imath\frac{\Omega}{2} - \frac{\epsilon}{2(1+\epsilon)}\left(\epsilon\lambda_0 - \frac{\imath}{\Omega}\right) + \imath\delta_N\frac{(1+\epsilon)}{2\Omega} - \mu_N\lambda_0\frac{(1+\epsilon)}{2} + \frac{3\imath K'_N}{4\Omega^3}(1+\epsilon)|\Phi_2|^2 \tag{25}$$

$$A_{24} = +\frac{3\imath K'_N}{8\Omega^3}(1+\epsilon)\Phi_2^2 \tag{26}$$

Stability of the fixed points is determined by calculating roots of the characteristic polynomial of the matrix of the system given in Equation (21). If all roots possess a negative real part, then the fixed point is stable. If a real root crosses the half complex plane, the fixed point is saddle-node.

If a pair of complex roots leaves the left part of the complex plane, there is a slow flow Hopf bifurcation.

Once amplitude $|\Phi_2^0|$ calculated, by writing $\Phi_2^0 = |\Phi_2^0| \exp(\imath\theta)$, it is easy to show that the phase θ is given by $\theta = \pi - \imath \ln(c_1|\Phi_2^0| + c_2|\Phi_2^0|^3)$. Then Φ_1^0 is calculated by solving Equation (11) for each value of Φ_2^0.

By introducing a detuning parameter σ such as $\Omega = 1 + \epsilon\sigma$, for $A = 10\ 000$ N, $\epsilon = 0.02$, $\mu_N = 0.2$, $\delta_N = 0.5$ and $K_N = 43$ it is simple to obtain the stable fixed points of the primary system displacement normalized by the forcing $|x^0|/F$, where it is recalled that $F = A/(m_N\omega_0^2)$, with and without nonlinear damping.The results are presented in Figure 6: $|x^0|/F = \left|(\Phi_1^0 + \epsilon\Phi_2^0)/(1+\epsilon)^2\right|/F$. In this figure, the center frequency, obtained for $\sigma = 0$ is $f_0 = \frac{\omega_0}{2\pi} \approx 0.5$ Hz corresponds to the frequency of the linear system without damping. The minimum frequency corresponding to $\sigma \approx -16$ is $f_{min} \approx 0.34$ Hz and the maximum frequency corresponding to $\sigma \approx +18$ is $f_{max} \approx 0.68$ Hz. In this figure, the gray curve corresponds to the primary system with NES without any nonlinear element, two peaks are visible: the highest at 0.51 Hz corresponds to the primary system, and the lowest at $\sqrt{\delta_N} \times 0.51 = 0.36$ Hz corresponds to the linear resonance of the NES. In Figure 6, the thick curves correspond to the stable fixed points while the thin curves correspond to the unstable fixed points. The blue curve is obtained for a nonlinear damping $\nu_N = 0$, showing a high amplitude spurious resonance below natural resonance of the primary system and a small stable detached resonance curve above natural resonance of the primary system. For intermediate values of the nonlinear damping, the continuous secondary low frequency high amplitude resonance curve splits into two stable branches, one at low frequency with low amplitude and one with high frequency and amplitude, this last one is that to be avoided. The green curve, obtained for a nonlinear damping $\nu_N = 800$ is an example of this splitting of detached resonance. In this case, a small detached resonance zone subsists around $\sigma = -1$ and the chosen nonlinear damping does not suffices to ensure a full control of the high amplitude detached resonance. The red curves are obtained for a nonlinear damping $\nu_N = 922$, the smallest value that cancels the high amplitude detached resonance curve. It is worth noting that in this case, it remains a small detached resonance but as it is fully unstable it does not present any problem.

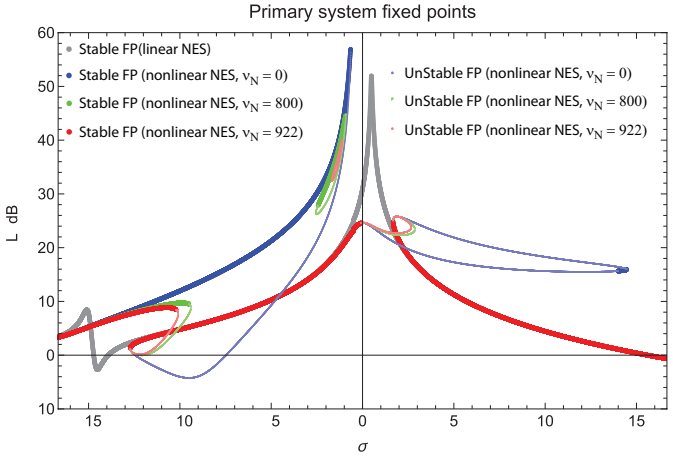

Figure 6: Stable (thick curves) and unstable (thin curves) fixed points of the primary system for $A = 10\ 000$ N, $\epsilon = 0.02$, $\mu_N = 0.2$, $\delta_N = 0.5$, $K_N = 43$, when varying ν_N.

It is worth noting that in this example the frequency range around main resonance of the primary system is twice-wider than that used in the optimisation process to show influence of the resonance of the NES at low frequency and high frequency detached resonance. From a practical point of view, it suffices to consider a 1/3 octave total frequency range to estimate the nonlinear damping necessary to cancel the detached resonance.

The fixed points on the main curve (here in red) around the main resonance of the primary system are identical whether linear damping is taken into account or not (the main resonance curves are merged). On the other hand, introducing the non-linear damping prevents the detached resonance without modifying the solution around the resonance of the linear system to be

controlled; in the present example, and also in all the examples tested, there is only a very slight difference in the calculated level (less than 1 dB) with and without nonlinear damping at the boundaries of the stable zone near the main resonance of the primary system, around $\sigma = 0$ and $\sigma = 2$ in Figure 6.

4.2 Slow invariant manifold

A very efficient way to attenuate the vibration is observed under Strongly Modulated Response (SMR) in the vicinity of the 1 : 1 resonance, see e.g. chapter 6 in (Vakakis et al. 2008). Two time scales $\tau_0 = \tau$ and $\tau_1 = \epsilon\tau$ appear naturally in this type of motion and a multi-scale asymptotic development to order 0 in ϵ allows us to obtain this manifold. Let us state $\Phi_i = \phi_i^0 + \epsilon\phi_i^1 + O(\epsilon^2)$, we obtain to the order 0 in ϵ the following set of differential equations:

$$\dot{\phi}_1^0 = 0 \tag{27}$$

$$\dot{\phi}_2^0 + \frac{\imath}{2}\left(\phi_2^0 - \phi_1^0\right) - \frac{\mu_N\lambda_0}{2}\phi_2^0 - \frac{3\imath\tilde{K}'_N}{8}|\phi_2|^2\phi_2 - \imath\frac{\delta_N}{2}\phi_2^0 = 0, \tag{28}$$

with $\tilde{K}'_N = K_N\left(1 - \nu_N\mu_N\lambda_0\frac{2}{3\imath K_N}\right)$. Equation (27) gives $\phi_1^0 = \phi_1^0(\tau_1, \tau_2, \cdots) = \phi_1$. The fixed point $\phi_2^0 = \phi_2$ of Equation (28) is solution of

$$\imath\left(\phi_2 - \phi_1\right) + \mu_N\lambda_0\phi_2 - \frac{3\imath\tilde{K}'_N}{4}|\phi_2|^2\phi_2 - \imath\delta_N\phi_2 = 0. \tag{29}$$

Let us write the fixed points under polar form $\phi_1 = \sqrt{Z_1}\exp(\imath\theta_1)$ and $\phi_2 = \sqrt{Z_2}\exp(\imath\theta_2)$. A few algebraic manipulations give the Slow Invariant Manifold (SIM) for 1 : 1 resonance capture:

$$Z_1 = \alpha_1 Z_2 + \alpha_2 Z_2^2 + \alpha_3 Z_2^3, \tag{30}$$

where the real coefficients $\alpha_i, i = 1, 2, 3$ are given by:

$$\alpha_1 = (\delta_N - 1)^2 + \lambda_0^2\mu_N^2, \tag{31}$$

$$\alpha_2 = \frac{3}{2}K_N(\delta_N - 1) - \nu_N\lambda_0^2\mu_N^2, \tag{32}$$

$$\alpha_3 = \frac{1}{16}\left(9K_N^2 + 4\nu_N^2\lambda_0^2\mu_N^2\right). \tag{33}$$

This SIM has one or three solutions. The bifurcation points are obtained by canceling the derivative of the second member of the equation (30) with respect to Z_2: $\alpha_1 + 2\alpha_2 Z_2 + 3\alpha_3 Z_2^2 = 0$. The two roots of this equation are :

$$Z_2^{(1)} = \frac{-\alpha_2 - \sqrt{\Delta}}{3\alpha_3}, Z_2^{(2)} = \frac{-\alpha_2 + \sqrt{\Delta}}{3\alpha_3}, \tag{34}$$

with $\Delta = \alpha_2^2 - 3\alpha_1\alpha_3$, one obtains:

$$\Delta = \frac{1}{4}\left[\left(3K_N(\delta_N - 1) - 2\nu_N\lambda_0^2\mu_N^2\right)^2 - \frac{3}{4}(1 + \lambda_0^2\mu_N^2 - 2\delta_N + \delta_N^2)(9K_N^2 + 4\nu_N^2\lambda_0^2\mu_N^2)\right]. \tag{35}$$

For $Z_2^{(1,2)}$ to exist, Δ must be positive. It is easy to see form Equation (35) that Δ is a polynomial of degree 2 in δ_N. Let us calculate the values $\delta_N^{(1,2)}$ that cancel Δ. One obtains:

$$\delta_N^{(1)} = 1 + \sqrt{3}\lambda_0\mu_N\left(\frac{1}{3} - \frac{4}{3 + 2\sqrt{3}\nu_N\lambda_0\mu_N/K_N}\right) \tag{36}$$

$$\delta_N^{(2)} = 1 - \sqrt{3}\lambda_0\mu_N\left(\frac{1}{3} - \frac{4}{3 - 2\sqrt{3}\nu_N\lambda_0\mu_N/K_N}\right) \tag{37}$$

Depending on the value of ν_N, two cases can be considered.

1. if $\nu_N = 0$ and $\sqrt{3}\lambda_0\mu_N < 1$,

$$\delta_N^{(1)} = 1 - \sqrt{3}\lambda_0\mu_N \tag{38}$$
$$\delta_N^{(2)} = 1 + \sqrt{3}\lambda_0\mu_N \tag{39}$$

one can show that $\Delta \leq 0$ for $\delta_N \in [\delta_N^{(1)}, \delta_N^{(2)}]$. Then, for Δ to be positive, one must impose $\delta_N \leq \delta_N^{(1)}$ or $\delta_N \geq \delta_N^{(2)}$. To ensure that $Z_2^{(1,2)} \geq 0$, it is easy to see from Equation (34), that α_2 must be negative and then, from Equation (32), δ_N can not be greater than 1. Then, one obtains the classical condition (Wu et al. 2021) that when the NES possesses a linear stiffness δ_N, it must satisfy $\delta_N < 1 - \sqrt{3}\lambda_0\mu_N$.

2. if $\nu_N \neq 0$, the procedure differs a little. It is worth noting that, depending on the parameters, $\delta_N^{(1)}$ is not always smaller than $\delta_N^{(2)}$. Let us denote $\nu_N^\delta = \frac{\sqrt{3}K_N}{2\lambda_0\mu_N}$, the value of nonlinear damping that makes $\delta_N^{(2)}$ singular. Different sub-cases are to be considered.

   (a) If $\nu_N < \nu_N^\delta$, one can show that $\Delta \leq 0$ for δ_N lying in the interval limited by $\delta_N^{(1)}$ and $\delta_N^{(2)}$. In the vicinity of ν_N^δ, let us consider $\nu_N = \nu_N^\delta(1-\eta)$, $\eta \ll 1$, one has

$$\delta_N^{(1)} \approx 1 - \frac{1}{\sqrt{3}}\lambda_0\mu_N(1+\eta) \to 1 - \frac{1}{\sqrt{3}}\lambda_0\mu_N \text{ for } \eta \to 0, \tag{40}$$
$$\delta_N^{(2)} \approx 1 + \frac{4}{\sqrt{3}\eta}\lambda_0\mu_N \to \infty \text{ for } \eta \to 0. \tag{41}$$

   Then, if $\lambda_0\mu_N/\sqrt{3} < 1$, we must impose that $\delta_N < \delta_N^{(1)}$ and with $\Delta > 0$ close to zero, to ensure that α_2 must be negative, from Equation (32) one has to impose $\frac{3}{2}K_N(\delta_N - 1) - \nu_N^\delta(1-\eta)\lambda_0^2\mu_N^2 + O(\eta^2) < 0$, then one obtains $\delta_N < 1 + \frac{1}{\sqrt{3}}\lambda_0\mu_N + O(\eta)$. This condition, together with $\delta_N < \delta_N^{(1)}$, gives that δ_N must satisfies $\delta_N < 1 - \frac{1}{\sqrt{3}}\lambda_0\mu_N$. Care must be taken when $\nu_N < \nu_N^\delta$ because when $\nu_N \to 0$, condition reads $\delta_N < 1 - \sqrt{3}\lambda_0\mu_N$ which can significantly differs from the condition $\delta_N < 1 - \frac{1}{\sqrt{3}}\lambda_0\mu_N$ if $\mu_N\lambda_0$ is not small.

   (b) if $\nu_N > \nu_N^\delta$, one can show that $\Delta \geq 0$ for δ_N lying in the interval limited by $\delta_N^{(1)}$ and $\delta_N^{(2)}$. In the vicinity of ν_N^δ, let us consider $\nu_N = \nu_N^\delta(1+\eta)$, $\eta \ll 1$, one has

$$\delta_N^{(1)} \approx 1 - \frac{1}{\sqrt{3}}\lambda_0\mu_N(1-\eta) \to 1 - \frac{1}{\sqrt{3}}\lambda_0\mu_N \text{ for } \eta \to 0, \tag{42}$$
$$\delta_N^{(2)} \approx 1 - \frac{4}{\sqrt{3}\eta}\lambda_0\mu_N \to -\infty \text{ for } \eta \to 0. \tag{43}$$

   Here again, if $\lambda_0\mu_N/\sqrt{3} < 1$, we must impose that $\delta_N < \delta_N^{(1)}$ and with $\Delta > 0$ close to zero, to ensure that α_2 must be negative, from Equation (32) one has to impose $\frac{3}{2}K_N(\delta_N - 1) - \nu_N^\delta(1-\eta)\lambda_0^2\mu_N^2 + O(\eta) < 0$, then one obtains $\delta_N < 1 + \frac{1}{\sqrt{3}}\lambda_0\mu_N + O(\eta)$. One finally obtains that δ_N must satisfies $\delta_N < 1 - \frac{1}{\sqrt{3}}\lambda_0\mu_N$. For the general case $\nu_N > \nu_N^\delta$, no simple rule is available. As a simple rule of the thumb, for ν_N not too large, choose at first approach $\delta_N < 1 - \frac{1}{\sqrt{3}}\lambda_0\mu_N$, then the criteria detailed above allow us to specify the theoretical limits, keeping in mind that this is an approximate resolution and therefore the effective solutions may differ, especially near the limiting cases $\nu_N \ll \nu_N^\delta$ or $\nu_N \gg \nu_N^\delta$.

The stability of the SIM is obtained by an usual linearisation of a complex perturbation around the fixed points of the system composed by Equation (27) and Equation (28). Without giving too much details, this leads to compute the roots of a third order characteristic polynomial given in Equation (44)

$$\begin{aligned} p(X) &= X^3 + \mu_N\lambda_0 X^2(1 - Z_2\nu_N) \\ &\quad - \frac{X}{64}(((-4 + 3Z_2K_N + 4\delta_N)(-4 + 9Z_2K_N + 4\delta_N) + 4\mu_N^2\lambda_0^2(4 + Z_2\nu_N(-8 + 3Z_2\nu_N))). \end{aligned} \tag{44}$$

If all roots have a real part less or equal to zero, the SIM is stable. The three roots of this polynomials are given by

$$X_1 = 0 \tag{45}$$

$$X_2 = \frac{1}{8}\left(4\mu_N\lambda_0(-1+\nu_N Z_2) + \sqrt{\Delta_X}\right) \tag{46}$$

$$X_3 = \frac{1}{8}\left(4\mu_N\lambda_0(-1+\nu_N Z_2) - \sqrt{\Delta_X}\right) \tag{47}$$

with $\Delta_X = -48Z_2K_N(1-\delta_N) - 16(1-\delta_N)^2 + Z_2^2(-27K_N^2 + 4\mu_N^2\lambda_0^2\nu_N^2)$. For $Z_2 \in]Z_2^{(2)}, Z_2^{(1)}[$, the SIM is always unstable. For $\nu_N \gg 1$, as in the general case $Z_2 \ll 1$, one has $\Delta_X < 0$ and one can approximate the real part of the roots X_2 and X_3 by $\mu_N\lambda_0(-1+\nu_N Z_2)/2$. Then, the SIM is unstable for $Z_2 > Z_2^\nu = 1/\nu_N$.

An interesting feature of the dependence of the SIM with respect to the nonlinear damping is that it can be shown that $\alpha_1 Z_2^{(1)} + \alpha_2\left(Z_2^{(1)}\right)^2 + \alpha_3\left(Z_2^{(1)}\right)^3 = 0$ for $\nu_N^0 = 3/2K_N/(1-\delta_N)$. For example, let us consider $\delta_N = 0.5$ and $K_N = 43$. One obtains $\nu_n^0 = 129$. The SIM is plotted in Figure 7 for the parameters $\epsilon = 0.02$, $\mu_N = 4$, $\delta_N = 0.5$ and $K_N = 43$ for $\nu_N = 0$ and $\nu_N = \nu_N^0$. In this figure, the black dots correspond to the bifurcation points $Z_2^{(1,2)}$; the red dot correspond to Z_2^ν.

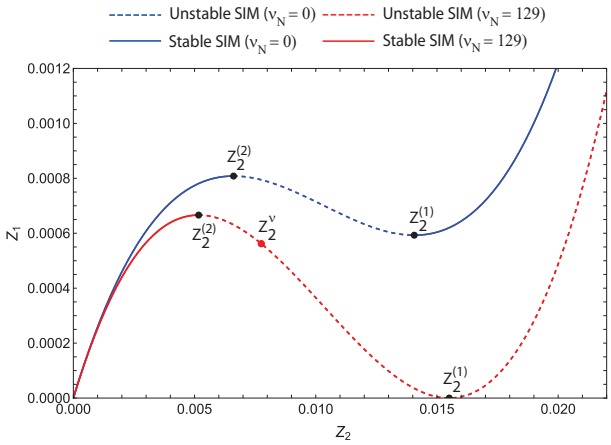

Figure 7: SIM for $\epsilon = 0.02$, $\mu_N = 4$, $\delta_N = 0.5$, $K_N = 43$, $\nu_N = 0$ and $\nu_N = 129$.

This feature of non-linear damping change dramatically the efficiency of the NES. As it is classical that too much damping can destroy SMR, the chosen value $\mu_N = 4$ in Figure 7, corresponding to a NES linear damping four times greater than linear system damping (even with such a high value, as $\lambda_0 = 0.1$, the strongest condition $\sqrt{3}\lambda_0\mu_N < 1$ is satisfied), allows a very short range of possible SMR when $\nu_N = 0$ while remaining maximum for $\nu_N = \nu_N^0$. As ν_N^0 does not depends on ϵ nor μ_N, it can not be used as a guide to choose the nonlinear damping that cancels detached resonance for a given ϵ and μ_N.

For the parameters $\epsilon = 0.02$, $\mu_N = 0.2$, $\delta_N = 0.5$ and $K_N = 43$, the value of nonlinear damping that destroy detached resonance for the maximum system forcing amplitude $A = 10000$ N is $\nu_N = 922$. It is worth noting that it suffices to cancel the detached resonance for the highest amplitude to ensure that it is canceled for all lesser amplitudes. We plotted the SIM for $\nu_N = 0$ and $\nu_N = 922$ in Figure 8. In this figure, whatever the value of the non-linear damping, relaxation oscillations (indicated by green arrows) are observed for which there is a possibility of SMR. The limiting values of Z_1 and Z_2 are given by $Z_1^* \approx 0.0058$ et $Z_2^* \approx 0.02$.

It is worth noting that in Figure 8, the significant nonlinear damping has modified the shape of the SIM in two ways: first, the bifurcation point $Z_2^{(1)}$ moves away from the abscissa axis, as it is classical for a damped system, for that case $\nu_N^0 = 129$ is far from the necessary nonlinear damping that cancels detached resonance; secondly, and more important, the SIM is stable only for $Z_2 \in [0, 1/\nu_N]$, which correspond only to a small part of of the SIM. In Figure 8, the black dots correspond to the bifurcation points $Z_2^{(1,2)}$ and Z_2^ν is indicated as a red dot.

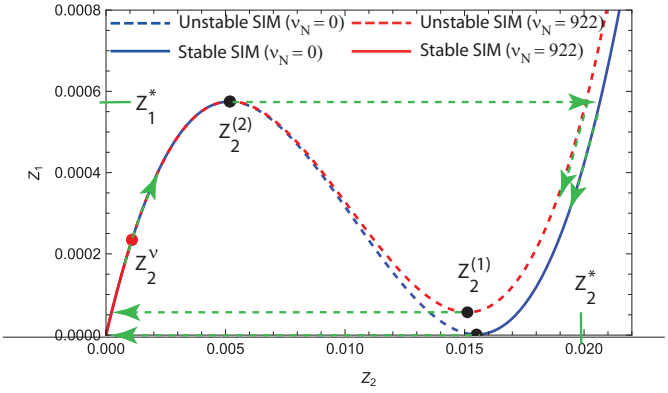

Figure 8: SIM for $\epsilon = 0.02$, $\mu_N = 0.2$, $\delta_N = 0.5$, $K_N = 43$, $\nu_N = 0$ or 922

4.3 Numeric simulations compared to the analytical results

Two kind of comparisons are presented in this section. The first deals with a comparison between the frequency response obtained from a numerical solution of the exact equation (always with 101 frequency points) and that obtained from the analytical solution given by Equations (11) and (12). The second deals with the projection of the numerical time signal onto the SIM given by Equation (30) for two different forcing.

The parameters common to all comparisons are: $\epsilon = 0.02$, $\mu_N = 0.2$, $\delta_N = 0.5$, $K_N = 43$.

4.3.1 Numeric simulations compared to the analytical result: frequency response function

A comparison between the frequency response function (i.e. the fixed points) obtained by integration of the numerical solution of the exact equations and the analytical solution when ν_N is taken to be zero or to the values that cancel stable detached resonance for a forcing $A = 9800$ N is shown in Figure 9. It is worth noting that, except for frequencies slightly greater than the resonance of the linear system (say $2 < \sigma < 6$) where some discrepancies occur, the exact and numerical solutions are very close. When two stable branches exist at a given frequency, the numerical solution may jump from one to the other, depending on initial conditions. An explanation for the observed discrepancy for frequencies above the resonance of the linear system is given in the next subsection, where its is shown that the solution jumps onto a different branch of periodic solution not predicted by the present analysis.

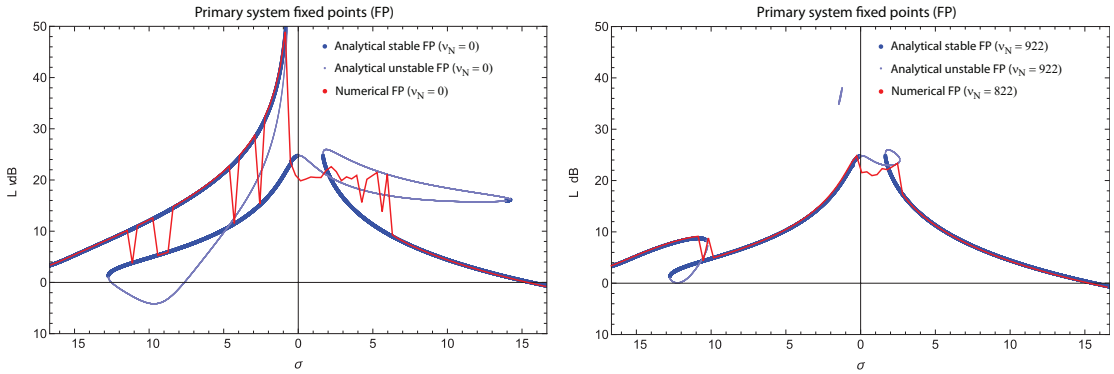

Figure 9: Stable (thick curves) and unstable (thin curves) fixed points of the primary system for $A = 9800$ N, $\epsilon = 0.02$, $\mu_N = 0.2$, $\delta_N = 0.5$, $K_N = 43$. Blue curves correspond to the analytical solution. Red curves correspond to the numerical solution. Left figure $\nu_N = 0$. Right figure $\nu_N = 922$ for the analytical solution or $\nu_N = 822$ for the numerical solution.

4.3.2 Numeric simulations compared to the analytical result: time signal projected onto the SIM

The second example deals with time motion resulting from the numerical solution of the problem equations. In a first example, plotted in Figure 10, the forcing had an amplitude $A = 9800$ N and frequency $f = 0.51$ Hz It is worth noting that, in the present case and for all calculations, slightly

different values of the nonlinear damping ν_N had been necessary to cancel detached resonance for numerical and analytical results. The projection of the time series onto the SIM is given in Figure 11.

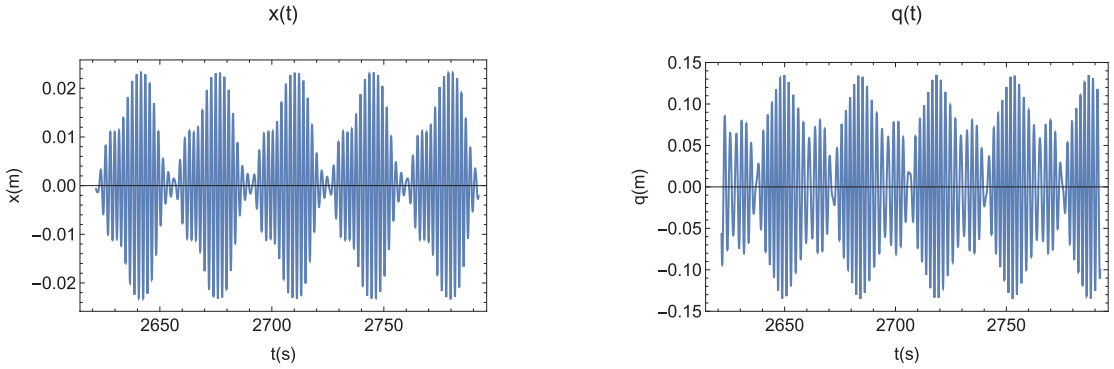

Figure 10: Example of time series $x(t)$ on the left and $q(t)$ on the right under SMR for $A = 9800$ N, $f = 0.51$ Hz, $\epsilon = 0.02$, $\mu_N = 0.2$, $\delta_N = 0.5$, $K_N = 43$ and $\nu_N = 822$.

The amplitude maxima correspond to those predicted by the SIM:

$$\max x(t) \approx 0.023 \quad \Rightarrow \quad (\max x(t))^2 \approx 0.0053 \approx Z_1^*, \tag{48}$$

$$\max q(t) \approx 0.135 \quad \Rightarrow \quad (\max q(t))^2 \approx 0.018 \approx Z_2^*. \tag{49}$$

A small plateau is observed for both the primary system $x(t)$, around $x(t) \approx 0.011$, that is $Z_1 \approx 0.00014$, and the NES $q(t)$, around $q(t) \approx 0.065$, that is $Z_2 \approx 0.0053$, in the SMR. It corresponds to the small plateau observed in Figure 11 roughly around the unstable point in the SIM given by Z_2^ν.

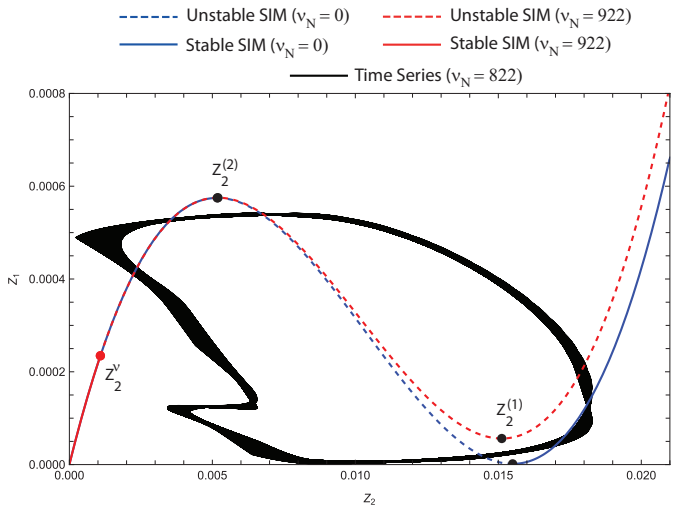

Figure 11: Projection of the time series onto the SIM for $A = 9800$ N, $f = 0.51$ Hz, $\epsilon = 0.02$, $\mu_N = 0.2$, $\delta_N = 0.5$, $K_N = 43$ and $\nu_N = 922$ for analytical calculation or $\nu_N = 822$ for numerical calculation.

While these results seem to be convincing, they must be pondered by the fact that for different forcing conditions, the predictions allowed by SIM under 1:1 resonance are less pertinent. For example, the motion resulting from the numerical solution of the problem equations for a forcing with amplitude $A = 9000$ N and frequency $f = 0.507$ Hz had been plotted in Figure 12.

In this example, the SMR shows two different shapes. When the times series is projected onto the SIM as shown in Figure 13, it is easy to see the system partially follows the SIM under 1:1 resonance given in Figure 11 and jumps regularly onto a different branch of periodic solution.

To have a better understanding of the nature of the transitions that occur, an Hilbert-Huang analysis (see Huang et al. 1998) is conduced on the time series. Without giving too much detail about the Hilbert-Huang transform (HHT), the core of this method is to decompose the signal into what's named empirical modes (so the name empirical mode decomposition - EMD). These

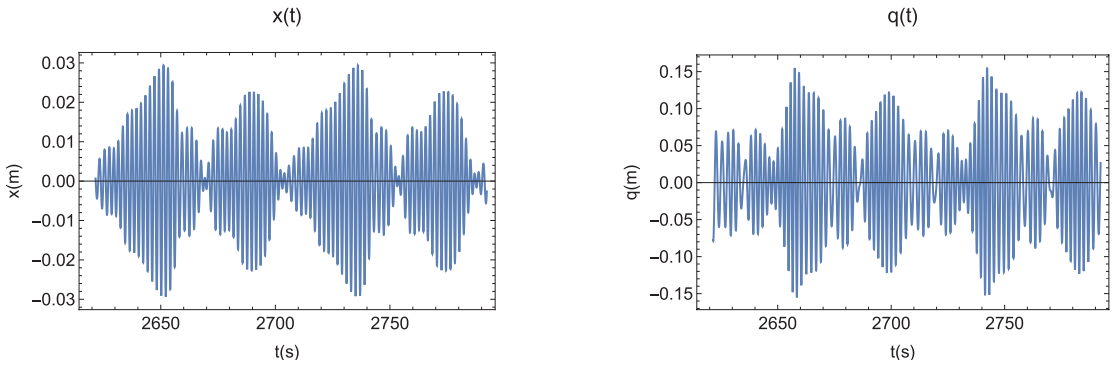

Figure 12: Example of time series $x(t)$ on the left and $q(t)$ on the right under SMR for $A = 9000$ N, $f = 0.507$ Hz, $\epsilon = 0.02$, $\mu_N = 0.2$, $\delta_N =$, $K_N = 43$ and $\nu_N = 922$ for analytical calculation or $\nu_N = 822$ for numerical calculation.

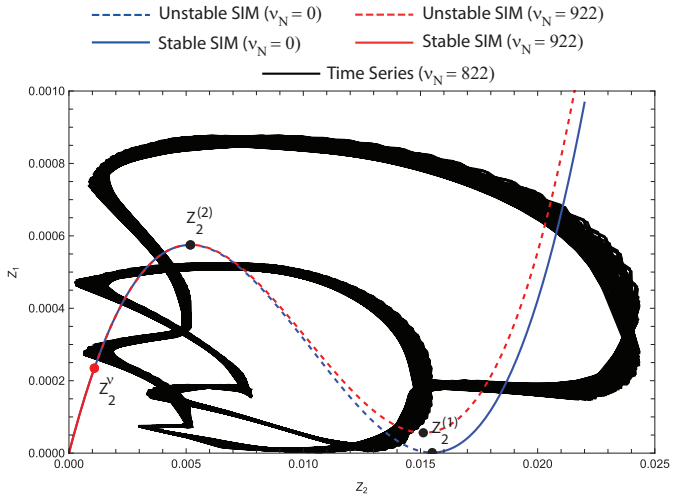

Figure 13: Projection of the time series onto the SIM for $A = 9000$ N, $f = 0.507$ Hz, $\epsilon = 0.02$, $\mu_N = 0.2$, $\delta_N = 0.5$, $K_N = 43$ and $\nu_N = 922$ for analytical calculation or $\nu_N = 822$ for numerical calculation.

based signal modes (the so called intrinsic mode function - IMF) split the signal into decreasing frequency component, each of it possessing by construction only one frequency component at a each time; then a Hilbert spectral analysis - HSA is conduced allowing to compute each IMF's instantaneous frequency. Generally a signal possesses less than 10 IMFs but 20 IMFs is possible on particularly rich signals.

One of the main difficulty of this method is the extraction of the IMFs and the program (a simple executable code working under Windows) proposed by Loudet (2009) allows fast and efficient EMD. For the times series given in Figure 10 and in Figure 12, less than 6 IMFs were necessary to analyze the signals and only the first three contain significant data. The results of HHT analysis of times series presented in Figure 10 is given in Figure 14 for the linear system displacement and in Figure 15 for the NES displacement. The results of HHT analysis of times series presented in Figure 12 is given in Figure 16 for the linear system displacement and Figure 17 for the NES displacement. In each of these figures, three sub-figures are given, the top is the corresponding IMF, the center colored figure is the wavelet analysis of the IMF and the bottom one is the instantaneous frequency obtained by HSA. It is worth noting that the instantaneous frequency curves have been plotted with the convention that the higher the IMF amplitude the darker the curve.

For the regular SMR, corresponding to the time series given in Figure 10, HHT of the linear system given in Figure 14 reveals that the motion during SMR occurs at the forcing frequency and no significant energy conversion is observed; the first IMF contains most of the energy of the linear system motion. At the transition between two bursts, the motion occurs at small amplitude (amplitude of IMF 2 is more or less a hundred less than that of IMF 1) and has a frequency mainly $f_0/3$ and with an even smaller component on IMF 3 (one third of IMF 2) with a frequency

$f_0/5$. HHT of the NES motion given in Figure 15, reveals similar comportment with obviously a significant frequency variation fo the NES and amplitude of the second IMF only ten times smaller than the first one with a frequency mainly at $f_0/3$. This indicate a 1:1 resonance capture during the SMR and a 1:3 resonance capture during transition between the two bursts.

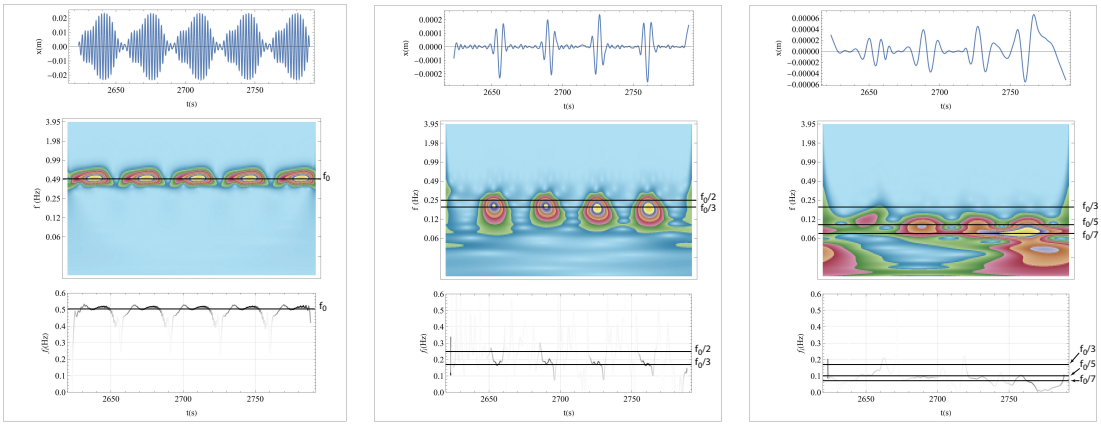

Figure 14: $x(t)$ first (left), second (middle) and third (left) IMF. $A = 9800$ N, $f = 0.51$ Hz, $\epsilon = 0.02$, $\mu_N = 0.2$, $\delta_N = 0.5$, $K_N = 43$ and $\nu_\Phi = 822$. Top: IMF, center: Wavelet analysis, bottom: instantaneous frequency.

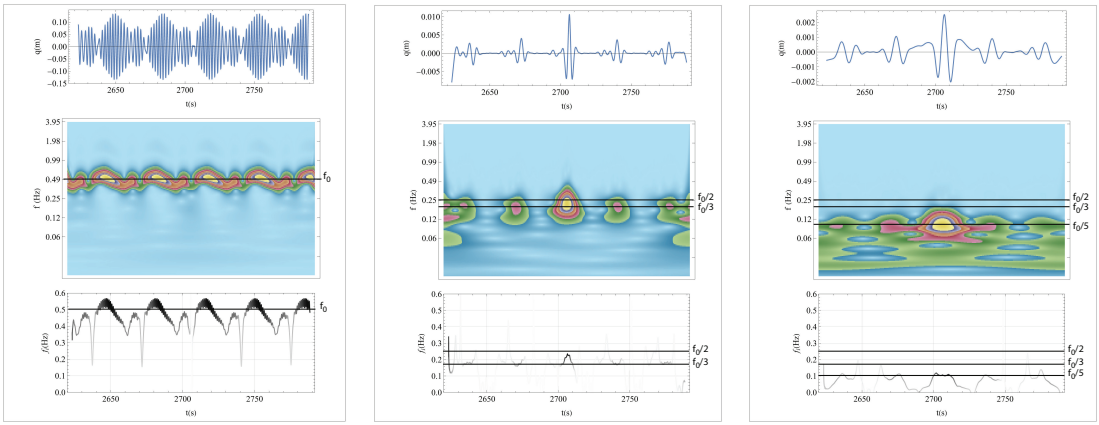

Figure 15: $q(t)$ first (left), second (middle) and third (left) IMF. $A = 9800$ N, $f = 0.51$ Hz, $\epsilon = 0.02$, $\mu_N = 0.2$, $\delta_N = 0.5$, $K_N = 43$ and $\nu_\Phi = 822$. Top: IMF, center: Wavelet analysis, bottom: instantaneous frequency.

For the double SMR, corresponding to the time series given in Figure 12, the HHT of the linear system given in Figure 16 reveals that the energy during the two kind of SMR is located at the forcing frequency and no significant energy conversion is observed; the first IMF contains most linear system motion energy. At the transition between two bursts, the motion arose at small amplitude (amplitude of IMF 2 is more or less a hundred less than that of IMF 1) and has a frequency mainly $f_0/2$ and with an even smaller component on IMF 3 (one third of IMF 2) with a frequency $f_0/5$. HHT of the NES motion given in Creffig:q(t)-IMF-1-2-A-9000-f-0.507, reveals similar comportment with obviously a significant frequency variation for the NES, an amplitude of the second IMF only ten times smaller than the first IMF with a frequency mainly at $f_0/3$. This indicate a 1:1 resonance capture during the SMR and a 1:2 resonance capture for the linear system and a 1:3 resonance capture for the NES during transition between two bursts. This could corresponds to the transient instability leading to 1:3 resonance capture observed by Andersen et al. (2012) with impulse with lower amplitude than that ensuring 1:1 resonance capture at high magnitude impulse. Obviously the systems under study differ by the forcing, impulse for Andersen et al. (2012) and continuous forcing in the present work. But, as noted by Andersen et al. (2012), *this instability is attributed solely to the passive nonlinear damping*. While further analytical studies would had been useful, this is not the core of this work and they are left to future work.

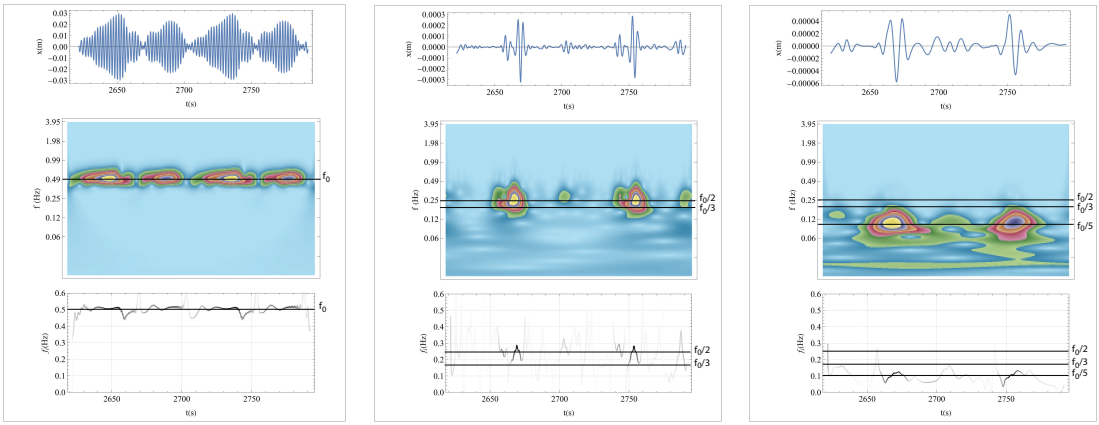

Figure 16: $x(t)$ first (left), second (middle) and third (left) IMF. $A = 9000$ N, $f = 0.507$ Hz, $\epsilon = 0.02$, $\mu_N = 0.2$, $\delta_N = 0.5$, $K_N = 43$ and $\nu_\Phi = 822$. Top: IMF, center: Wavelet analysis, bottom: instantaneous frequency.

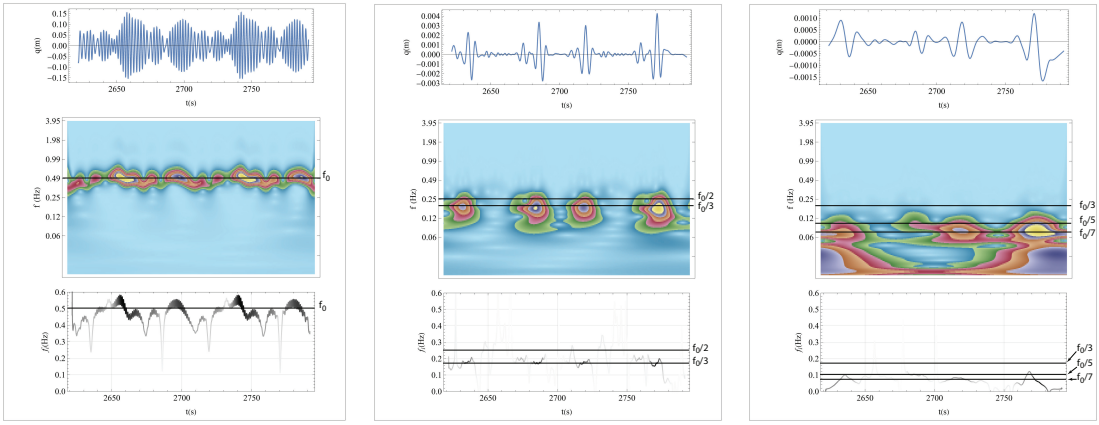

Figure 17: $q(t)$ first (left), second (middle) and third (left) IMF. $A = 9000$ N, $f = 0.507$ Hz, $\epsilon = 0.02$, $\mu_N = 0.2$, $\delta_N = 0.5$, $K_N = 43$ and $\nu_\Phi = 822$. Top: IMF, center: Wavelet analysis, bottom: instantaneous frequency.

All these results clearly show that accounting for nonlinear damping, while modifying the behavior of the system by removing the detached resonances, does not fundamentally alter the nature of the coupling between primary system and NES.

5 Optimisation results

We proceeded to the minimization of function J defined in equation (6) of more than a hundred different configurations obtained by fixing ϵ and μ_N for $\epsilon \in [0.001, 0.05]$ and $\mu_N \in [0.1, 1]$ and by looking for the values of δ_N and K_N which allowed the greatest average attenuation over the whole range of forcing of the wind turbine. Once these estimates have been done, and this corresponds to the heaviest computational part of the work as each configurations takes around three days of parallel computation, one looks for the smallest value of ν_N which avoided the phenomenon of detached resonance; such an estimate is easy to do as the analytical result gives a precise estimate of the actual value.

While not all details are reported here, it is to be noticed that, particularly for small values of ϵ, multiple combinations (2 or 3) of K_N and δ_N lead to comparable values for attenuation. As is in such case it becomes very difficult to estimate an absolute minimum, we decided to choose identified values that ensure, when possible, a regular evolution with respect to the parameters ϵ and μ_N.

An example of multiple minima of J, as defined in equation (6), is given in Figure 18. In this figure, we present a 3D plot and a contour plot of $20 \log |J|$ versus $\delta_N \in [0; 1]$ and $K_N \in [0; 40]$ for $\epsilon = 0.004$ and $\mu_N = 0.3$. In this figure only negative values of J, corresponding to an reduction

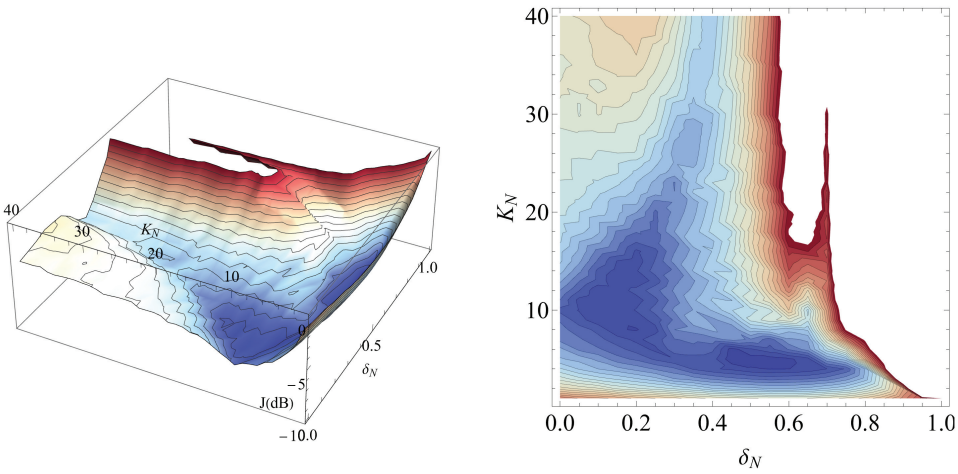

Figure 18: Map of J as a function of δ_N and K_N for $\epsilon = 0.004$ and $\mu_N = 0.3$. Left: 3-D plot, right: contour plot

of vibration of primary system, have been plotted. This shows that two separated minima exist, the first in the vicinity $\delta_N \approx 0.5$, $K_N \approx 5$ and the second in the vicinity of $\delta_N \approx 0.2$, $K_N \approx 8$. A refined study around these two points gives

$$\delta_N = 0.48, K_N = 5.4 \implies J = -8 \text{ dB}, \tag{50}$$

$$\delta_N = 0.19, K_N = 8.1 \implies J = -7.7 \text{ dB}, \tag{51}$$

while comparable, the first minimum given in (50) gives a slightly better attenuation and a more smooth variation of δ_N and K_N when ϵ and μ_N vary. It have then be chosen. It is worth noting that for significant range of δ_N and K_N, represented in white in Figure 18, the parameter choice leads to a positive value of J meaning a increase in the response of the linear system that must absolutely avoided. As it has been shown, the linear stiffness must satisfies $\delta_N < 1 - \sqrt{3}\lambda_0\mu_N$, and in the present case, with $\lambda_0 = 0.1$, and $\mu_N = 0.3$, one must have $\delta_N < 0.95$. This limit is observed in the right sub-figure in Figure 18, where whatever K_N, if $\delta_N > 0.95$ then $J > 0$ and the chosen parameters lead to a NES unable in reducing the vibration of the primary linear system.

The results are presented in Figure 19 for δ_N (left sub-figure) and K_N (right sub-figure); in this figure, we presented the parameters δ_N and K_N versus ϵ which give the best attenuation imposing zero initial conditions for different NES linear damping μ_N. It is obvious that for small values of ϵ (say less that 0.5%), both δ_N and K_N show significant variations while becoming more smooth and regular for $\epsilon > 1\%$. For sufficiently high values of ϵ, both parameters show a power dependence with respect to ϵ and μ_N; while not completely clear for δ_N, its obvious for K_N. This will be precised later on.

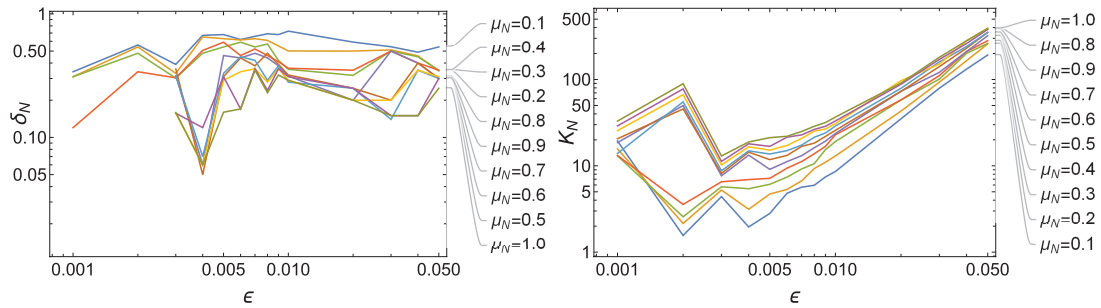

Figure 19: Identified optimal parameter values vs ϵ for different linear damping μ_N. Left: δ_N, right: K_N.

To ensure that solutions will bifurcate onto detached resonance, non zero initial conditions are imposed, and the values of nonlinear damping that cancel it for the highest forcing A_{max} are given in Figure 20. In this figure, the results are presented for analytical approximated solution

(left sub-figure) denoted ν_N^a and for numeric simulation of the exact solution (right sub-figure) denoted ν_N^c. Here again, it is clear that for small values of ϵ (say less that 1%), both nonlinear damping obtained from analytical ν_N^a and numeric ν_N^c estimates show significant variations while becoming more smooth and regular for $\epsilon > 1\%$ with comparable numeric values. Without giving too much details, these variations are observed when the function to minimize J possesses more than one minimum and when one of this minimum vanishes or appears when ϵ varies. It is to be remarked that for very low values of ϵ (less that 2%), there is no clear detached resonance and nonlinear damping is useless; but in that case, the NES does not allow an efficient vibration control of the primary linear system (only a few dB) and, combined with high variation in the identification coefficient, the solution with very small ϵ must not be considered as efficient.

As observed for δ_N and K_N, that both parameter ν_N^a and ν_N^c show a power dependence with respect to ϵ and μ_N. For the highest values of ϵ, analytical and computed coefficients of nonlinear damping obtained show significantly high values. However, it must be kept in mind that the damping of the NES is given by $\epsilon\mu_N\lambda_0(1 + 2\nu_N w^2(t))\dot{w}(t)$ with $\lambda_0 = 0.1$ for $\epsilon = 0.01$ and $\mu_N \in [0.1, 1]$. In fact, even if the values of ν_N seem high, the values of $\epsilon\mu_N\lambda_0\nu_N$ remain in acceptable orders of magnitude. To confirm this, let us define a NES mass $m_N = \epsilon m_0 = 10000$ kg and $\mu_N = 0.5$. With $\epsilon = 0.01$, one has $\lambda_0 = c_0/(m_N\omega_0) \approx 0.1$, the optimal values of ν_N is 68 for the numeric computation of the exact equation and 85 for the analytical solution, then we take $\nu_N \approx 80$. For $\mu_N = 0.5$, that is a linear NES damping of half that of the primary system, one has $c_N = 1600$ N.s/m. The non linear damping coefficient is then $2\nu_N c_N \approx 260\,000$ N.s/m, corresponding, for a linear frequency of 0.5 Hz, to an approximate linear damping of $\zeta_N = 2\nu_N c_N/(2m_N\omega_0) \approx 4.$.

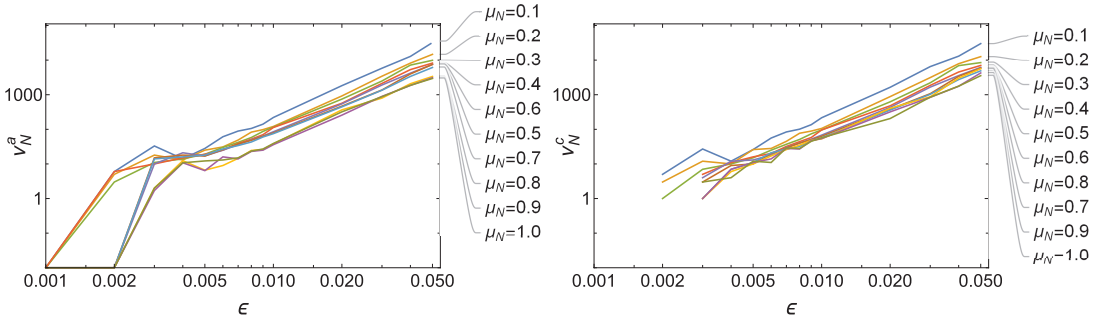

Figure 20: Identified optimal nonlinear damping versus ϵ for different linear damping μ_N. Left: analytical ν_N^a, right: numeric computation ν_N^c.

Finally, we present in Figure 21 the best average gain obtained as a function of the mass ϵ and damping μ_N. In this figure L(dB) represents the mean level of root mean square value for the linear system normalized by the mean level of root mean square value for the linear system without nonlinear dependence in both stiffness and damping, The value is calculated in decibel over the whole amplitude range $A \in [0, 10\,000]$ N. The best attenuation (up to 21 dB mean average attenuation) is obtained for the NES with highest mass and lowest damping. Here again, the attenuation becomes more smooth and regular for $\epsilon > 1\%$

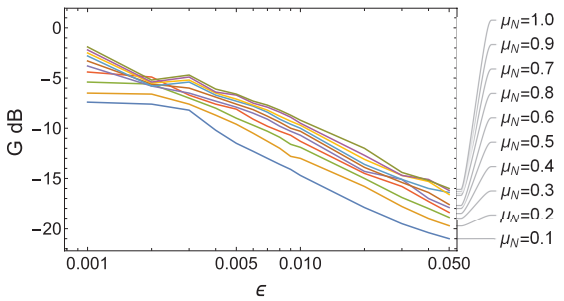

Figure 21: Best average gain obtained for various NES linear damping.

All these regular curves in logarithmic plots results suggest, except for the lowest values of ϵ, a dependence of the parameters as function of powers of ϵ and μ_N. The identification conduced

on the whole data set leads to the following results:

$$\begin{aligned} G_{dB} &\approx C_G \cdot \epsilon^{1/3} \mu_N^{-1/6}, C_G \approx -43.1 && (52)\\ K_N &\approx C_K \cdot \epsilon^{3/2} \mu_N^{1/3}, C_K \approx 35150 && (53)\\ \nu_N^a \approx \nu_N^c &\approx C_\nu \cdot \epsilon^3 \mu_N^{-1}, C_\nu \approx 2.5.10^7 && (54)\\ \delta_N &\approx C_\delta \cdot (1 + \alpha_1 \epsilon + \alpha_2 \epsilon^2)(1 + \beta_1 \mu_N + \beta_2 \mu_N^2), && (55) \end{aligned}$$

with for $0.001 \leq \epsilon < 0.009$, $C_\delta \approx 0.063$, $\alpha_1 \approx 3329.5$, $\alpha_2 \approx -228301$, $\beta_1 \approx -1.2$ and $\beta_2 \approx 0.47$ and for $0.009 \leq \epsilon \leq 0.05$, $C_\delta \approx 0.77$, $\alpha_1 \approx -11.5$, $\alpha_2 \approx 144.11$, $\beta_1 \approx -1.3$ and $\beta_2 \approx 0.65$.

The obtained values for the optimal nonlinear damping are almost identical for analytical and numerical solution and can be described by the same power law. This is an indication that analytical approximation obtained under 1:1 resonance assumption suffices to describe the cancellation of detached resonances by nonlinear damping.

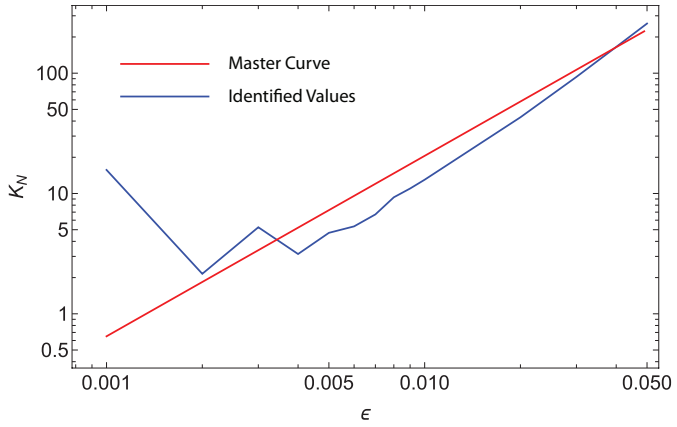

Figure 22: Comparison of a master curve and the identified values for K_N vs ϵ for $\mu_N = 0.2$

An example of comparison of a master curve and the identified values for K_N vs ϵ for $\mu_N = 0.2$ is given in Figure 22. Except ϵ lowest values, where the strongest fluctuations had been observed, the results are satisfactory and at least sufficient to give an initial value to more refined calculations.

6 Conclusion

This work was dedicated to the vibration mitigation of a simplified model of a FOWT by a NES with both linear and nonlinear stiffness and damping. We have shown that tuning NES nonlinear viscous damping allows to completely eliminate the detached resonances of the system and to keep absorber capacity to strongly limit the vibrations of the wind turbine over its whole operating range.

Furthermore, we have shown that classical tools of nonlinear dynamics (fixed points, SIM) can easily take into account this type of nonlinear damping and conduct fast analytical studies. We have shown that most of the dynamic of the system is conserved when nonlinear damping is added to the system. In particular, the fixed points of the principal frequency response curve are marginally modified when nonlinear damping is added to destroy detached resonances. Most of the influence of the nonlinear damping was observed on the SIM which shape remains mostly unaltered when nonlinear damping is accounted for, except its stability and for the particular values ν_N^0 that cancel the SIM at the bifurcation point $Z_2^{(1)}$. But, for the case under consideration in the present work with very small damping, $Z_2^{(1)}$ remains very close to zero and this property is not of particular interest. Nevertheless, for higher values of primary system damping this could be a useful feature.

By using a two steps optimisation procedure we were able to define parameters that strongly limit the vibration of the simplified model of FOWT over its whole excitation range and a significant frequency range. The first step consists in imposing zero initial condition and optimize linear and cubic stiffness for various NES mass and linear damping by minimizing the FOWT

ridge curve over its whole excitation range. The second step consists in, after computation of optimal parameters, estimating the nonlinear damping of the NES that cancel the detached resonance for the maximum amplitude.

The parametric study reveals that the parameters, say linear and nonlinear stiffness, attenuation and nonlinear damping depend upon simple power laws in NES mass and linear damping. This simple result is sufficient for NES dimensioning or at least can be used as estimate to more refined optimisation process.

Bibliography

Abramson, H. N. (1955). "Response Curves for a System With Softening Restoring Force". *Journal of Applied Mechanics* 22, pp. 434–435. DOI: 10.1115/1.4011105

Alexander, N. A. and F. Schilder (2009). "Exploring the performance of a nonlinear tuned mass damper". *Journal of Sound and Vibration* 319, pp. 445–462. DOI: 10.1016/j.jsv.2008.05.018

Andersen, D., Y. Starosvetski, A. F. Vakakis, and L. Brergman (2012). "Dynamic instabilities in coupled oscillators induced by geometrically nonlinear damping". *Nonlinear Dynamics* 67, pp. 807–827. DOI: 10.1007/s11071-011-0028-0

Bakre, S. V. and R. S. Jangid (2007). "Optimum parameters of tuned mass damper for damped main system". *Structural Control and Health Monitoring* 14.3, pp. 448–470. DOI: 10.1002/stc.166

Bellet, R., B. Cochelin, P. Herzog, and P.-O. Mattei (2010). "Experimental study of targeted energy transfer from an acoustic system to a nonlinear membrane absorber". *Journal of Sound and Vibration* 329, pp. 2768–2791. DOI: 10.1016/j.jsv.2010.01.029

Chen, Y.-Y., Z.-C. Qian, W. Zhao, and C.-M. Chang (2020). "A magnetic Bi-stable nonlinear energy sink for structural seismic control". *Journal of Sound and Vibration* 473, p. 115233. DOI: 10.1016/j.jsv.2020.115233

Den Hartog, J. P. (1947). *Mechanical Vibrations, Third Edition*. McGraw-Hill Book Compagny

Ding, H. and L.-Q. Chen (2020). "Designs, analysis, and applications of nonlinear energy sinks". *Nonlinear Dynamics* 100, pp. 3061–3107. DOI: 10.1007/s11071-020-05724-1

Gendelman, O., L. Manevitch, R. M'Closkey, and A. F. Vakakis (2001). "Energy Pumping in Nonlinear Mechanical Oscillators: Part I—Dynamics of the Underlying Hamiltonian Systems". *Journal of Applied Mechanics* 68, pp. 34–41. DOI: 10.1115/1.1345524

Gendelman, O., T. Sapsis, A. F. Vakakis, and L. A. Bergman (2011). "Enhanced passive targeted energy transfer in strongly nonlinear mechanical oscillators". *Journal of Sound and Vibration* 330, pp. 1–8. DOI: 10.1016/j.jsv.2010.08.014

Gourc, E., G. Michon, S. Seguy, and A. Berlioz (2014). "Experimental Investigation and Design Optimization of Targeted Energy Transfer Under Periodic Forcing". Vol. 136. 2, pp. 021021-1–8. DOI: 10.1115/1.4026432

Gourc, E., G. Michon, S. Seguy, and A. Berlioz (2015). "Targeted Energy Transfer Under Harmonic Forcing With a Vibro-Impact Nonlinear Energy Sink: Analytical and Experimental Developments". *Journal of Vibration and Acoustics* 137, p. 031008. DOI: 10.1115/1.4029285

Habib, G., G. I. Cyrillo, and G. Kerschen (2018). "Isolated resonances and nonlinear damping". *Nonlinear Dynamics* 96, pp. 979–994. DOI: 10.1007/s11071-018-4240-z

Habib, G. and F. Romeo (2020). "Comparative Analysis of NES and TMD Performance via High-Dimensional Invariant Manifolds". *IUTAM Symposium on Exploiting Nonlinear Dynamics for Engineering Systems*. Ed. by I. Kovacic and S. Lenci. Cham: Springer International Publishing, pp. 143–153. DOI: 10.1007/978-3-030-23692-2_13

Huang, N. E., Z. Shen, S. R. Long, M. C. Wu, H. H. Shih, Q. Zheng, N.-C. Yen, C. C. Tung, and H. H. Liu (1998). "The empirical mode decomposition and the Hilbert spectrum for nonlinear and non-stationary time series analysis". *Proc. R. Soc. Lond. A.* 454, pp. 903–995. DOI: 10.1098/rspa.1998.0193

Liu, Y., A. Mojahed, L. A. Bergman, and A. F. Vakakis (2019). "A new way to introduce geometrically nonlinear stiffness and damping with an application to vibration suppression". *Nonlinear Dynamics* 96, pp. 1819–1845. DOI: 10.1007/s11071-019-04886-x

[SW] Loudet, L., *Application of Empirical Mode Decomposition to the detection of Sudden Ionospheric Disturbances by monitoring the signal of a distant Very Low Frequency transmitter* version 1, 2009. URL: https://sidstation.loudet.org/emd-en.xhtml

Pahn, T., R. Rolfes, J. Jonkman, and A. Robertson (2012). "Inverse Load Calculation of Wind Turbine Support Structures - A Numerical Verification Using the Comprehensive Simulation Code FAST: Preprint (Revised)". *53rd AIAA/ASME/ASCE/AHS/ASC Structures, Structural Dynamics, and Materials Conference* (Apr. 23–26, 2012). AIAA. Honolulu, Hawaii. DOI: 10.2514/6.2012-1735

Rauscher, M. (1938). "Steady Oscillations of Systems With Nonlinear and Unsymmetrical Elasticity". *Journal of Applied Mechanics* 5.4, A169–A177. DOI: 10.1115/1.4008875

AL-Shudeifat, M. A. (2014). "Highly efficient nonlinear energy sinks". *Nonlinear Dynamics* 76, pp. 1905–1920. DOI: 10.1007/s11071-014-1256-x

Starosvetsky, Y. and O. V. Gendelman (2008). "Attractors of harmonically forced linear oscillator with attached nonlinear energy sink. II: Optimization of a nonlinear vibration absorber". *Nonlinear Dynamics* 51, pp. 47–57. DOI: 10.1007/s11071-006-9168-z

Starosvetsky, Y. and O. V. Gendelman (2009). "Vibration absorption in systems with a nonlinear energy sink: Nonlinear damping". *Journal of Sound and Vibration* 324, pp. 916–939. DOI: 10.1016/j.jsv.2009.02.052

Vakakis, A. F., O. V. Gendelman, L. A. Bergman, D. M. McFarland, G. Kerschen, and Y. S. Lee (2008). *Nonlinear Targeted Energy Transfer in Mechanical and Structural Systems*. Springer Dordrecht. DOI: 10.1016/j.jsv.2009.02.052

Wang, J., N. E. Wierschem, B. F. Spencer, and X. Lu (2015). "Track Nonlinear Energy Sink for Rapid Response Reduction in Building Structures". *Journal of Engineering Mechanics* 141, p. 04014104. DOI: 10.1061/(ASCE)EM.1943-7889.0000824

[SW] Wolfram Research, Inc., *Mathematica 13.0* version 13, 2021. URL: https://www.wolfram.com

Wu, Z., S. Seguy, and M. Paredes (2021). "Basic Constraints for Design Optimization of Cubic and Bistable Nonlinear Energy Sink". *Journal of Vibration and Acoustics* 144.2. DOI: 10.1115/1.4051548

Zuo, H., K. Bi, and H. Hao (2020). "A state-of-the-art review on the vibration mitigation of wind turbines". *Renewable and Sustainable Energy Reviews* 121, p. 109710. DOI: 10.1016/j.rser.2020.109710

Zuo, H. and S. Zhu (2022). "Development of novel track nonlinear energy sinks for seismic performance improvement of offshore wind turbine towers". *Mechanical Systems and Signal Processing* 172, p. 108975. DOI: 10.1016/j.ymssp.2022.108975